arXiv:astro-ph/9805249v1 19 May 1998

FLOWS IN SUNSPOT PLUMES DETECTED WITH SOHO

N. Brynildsen, P. Maltby, P. Brekke, T. Fredvik, S. V. H. Haugan,
O. Kjeldseth-Moe, and Ø. Wikstøl

Institute of Theoretical Astrophysics, University of Oslo, P.O. Box 1029 Blindern, 0315 Oslo, Norway

ABSTRACT

Bright EUV sunspot plumes have been observed in eight out of eleven different sunspot regions with the Coronal Diagnostic Spectrometer – CDS on SOHO. ¿From wavelength shifts we derive the line-of-sight velocity, relative to the average velocity in the rastered area, $120'' \times 120''$. In sunspot plumes we find that the motion is directed away from the observer and increases with increasing line formation temperature, reaches a maximum between 15 and 41 km s^{-1} close to log T $\approx$ 5.5, then decreases abruptly. The flow field in the corona is not well correlated with the flow in the transition region and we discuss briefly the implication of this finding.

Subject headings: Sun: corona — Sun: transition region — Sun: UV radiation — sunspots

1. Introduction

Foukal et al. (1974) introduced the notation "sunspot plumes" to describe areas above sunspot umbrae that are "the brightest features in an active region by an order of magnitude". This led to the idea that sunspot plumes are regions within large magnetic loops, extending to altitudes of several thousand kilometers above the photosphere, in which the temperature is one to two orders of magnitude lower than in the corona of the surrounding active region (Noyes et al. 1985). In contrast, based on numerous sunspot observations with the Ultraviolet Spectrometer and Polarimeter (UVSP) on the *Solar Maximum Mission (SMM)* Gurman (1993) found that sunspot plumes were nearly nonexistent. Most recently Maltby et al. (1998) observed sunspot plumes in five out of nine sunspot regions with the Coronal Diagnostic Spectrometer (CDS; Harrison et al. 1995) on the *Solar and Heliospheric Observatory (SOHO)* and discussed briefly previous conflicting results. The CDS observations showed that sunspot plumes exist in the upper part of the transition region, occur both in magnetic unipolar and bipolar regions, and may extend outside the umbra and into the penumbra.

¿From the energy requirements in sunspot loops Foukal (1976) suggested that rapid downflows occur in the plumes. Strong downflows over sunspots were reported by Brueckner, Bartoe, & VanHoosier (1977) and studied by Nicolas et al. (1982), while Kjeldseth-Moe et al. (1988) found that both upflows and downflows occurred. Other investigations have confirmed and extended these observations, for a review see Maltby (1997). None of the observations above referred specifically to plumes and to our knowledge the velocity in sunspot plumes is not known. An investigation by Brynildsen et al. (1998) on the connection between line emission and wavelength shift in sunspot regions may, however, hold some relevance to this. In this paper we extend the CDS material to twelve sunspot regions and present the first measurements of velocities in sunspot plumes.

2. Observations and Data Reduction

Observations of twelve sunspot regions, listed in Table 1, were obtained with the Normal Incidence Spectrometer (NIS) of the CDS instrument as part of a joint observing program on *SOHO*. Since NOAA 7981 recurs as NOAA 7986 eleven different regions were observed. A large fraction of the observing time was used to raster an area of $120'' \times 120''$, moving the narrow $2.0''$ spectrometer slit perpendicular to the slit direction in steps of $2.0''$. The exposure time was 20 s; each raster required 25 min and contains information from 60 adjacent slit locations for ten emission lines. The observations contain spectra with spectral resolution, $\lambda/\delta\lambda$, in the range 3635 – 4500 within ten narrow spectral windows centered on the selected lines, which cover a wide range of ionization temperatures, see Table 2. White light sunspot contours are taken from the MDI instrument (Scherrer et al. 1995) on SOHO and the National Solar Observatory. To compensate for the influence of solar rotation on the alignment, the images were re-aligned by moving the frequently observed MDI magnetograms artificially to the same observing time as the CDS recordings.

The data acquisition and detector characteristics that are relevant for this study were described by Harrison et al. (1995). Briefly, the CDS data are corrected for geometrical distortions, the CCD readout bias is removed, the non-wavelength-dependent calibration parameters peculiar to the detector are applied, including the exposure time, the amplification of the microchannel plate, and a flat-field correction. The final step in the calibration is to convert the photon events into absolute intensity units.

A careful approach to the line-of-sight velocity determination is required to avoid the possible influence of other lines within the spectral windows, particularly in areas where the line of primary interest is weak. Detailed investigations of the line profiles show that most of them may be represented with a single Gaussian profile. The profile parameters for He I λ584 and O III λ599 are determined in this way since no disturbing lines are found. We find that it is possible to improve the line-of-sight determination for the other lines by representing the observations by a composite line profile, comprised of two Gaussian components, where one Gaussian is adjusted to fit the line of primary interest and the other accounts for the second most intense line within the spectral window, see Table 2. This approach is used even in cases where the distance between the lines is too large to consider the second most intense line as a blend. After exploring different ways of reducing the data, we decided to use two, slightly different methods. In the first method the line profile parameters for both lines are determined by a least squares fit to the observations. This requires good signal to noise ratio both for the line and the blend and is applied to the

Mg IX λ368 line. In the second method we locate parts of the rastered area where the line of primary interest is weak and use this location to determine the wavelength position and line width of the second line. Keeping these parameters constant, we are able to fit the observations with a composite line profile. This method is tested by applying it to the He I λ522 line and compare the results with those obtained for the strong He I λ584 line, which is not influenced by other lines. We estimate the accuracy in the line-of-sight velocity determinations to be 5 km s^{-1} for He I λ584 and O V, 10 km s^{-1} for Mg IX, and 15 km s^{-1} for O III, O IV, Ne VI and Fe XVI.

3. Results

Following Maltby et al. (1998) we set the criterion for the presence of a sunspot plume by requiring that the contours for peak line intensity $I \geq 5 \times \overline{I}$ are located (1) above the umbra or part thereof and (2) with most of the emission inside the white light sunspot. Figure 1 (Plate L00) shows the observed spatial distribution of Ne VI λ562 peak line intensity in twelve sunspots. The brightest features with peak line intensity, I larger than 5 times the average intensity, $\overline{I}$, are encircled by yellow contours, whereas medium bright features with $I > 2.5 \times \overline{I}$ are encircled by green contours. NOAA 7973, 7986, 8073, 8083, 8085, 8113 and 8123 satisfy the adopted criterion for containing a sunspot plume. We also regard NOAA 8011 as containing a sunspot plume since the O V λ629 peak line intensity exceeds $5 \times \overline{I}$ in a small region above the umbra. It should be remarked that sunspots without plumes, NOAA 7981, 7999, 8076 and 8108, also show Ne VI λ562 peak line intensity $I > 5 \times \overline{I}$ both above and outside the sunspot. Since NOAA 7981 recurs as 7986 we note that Figure 1 (Plate L00) illustrates a finding of previous observers (e.g. Foukal 1976), that plumes may be absent during part of the sunspot's lifetime.

A remarkable feature in Figure 1 (Plate L00) is that the enhanced Ne VI emission appears to outline one or a few thin emission structures, extending from the sunspot to the surrounding regions. In NOAA 8076 the extended feature resembles a magnetic loop, but in other regions, such as NOAA 7986, the medium bright emission features look like footpoints of magnetic loops. Similar features emitting strongly in the transition region lines O IV λ554 and O V λ629 are observed in almost the same locations. We note that Foukal (1976) remarked that strong cool emission was often found near both foot points of a loop, even if only one foot point could be confidently traced to the umbra. This suggests that Foukal (1976) observed similar emission structures to those seen in Figure 1 (Plate L00).

We now consider the line-of-sight velocity in bright areas above sunspots, i.e. areas encircled with yellow contours in Figure 1 (Plate L00) both in sunspot plumes and in equally bright areas above the other sunspots. Figure 2 shows the relative line-of-sight velocity, v, versus line formation temperature, T, in these bright areas above sunspots. Since most of the sunspots are observed close to the disk centre we tend to use the words upflow and downflow, even though contributions from horizontal velocities cannot be excluded. The CDS spectra contain few chromospheric lines and therefore the line-of-sight velocity is measured relative to the average line-of-sight velocity in the rastered area, $120'' \times 120''$. No corrections for the differential redshift between transition region- and chromospheric lines are applied.

Figure 2 shows that the relative line-of-sight velocity is directed away from the observer and increases with increasing temperature, reaches a maximum between 15 and 41 km s^{-1} close to log T $\approx$ 5.5 and then decreases abruptly. For nine out of twelve sunspots the maximum relative velocity exceeds 26 km s^{-1}. The result is valid both for sunspot plumes and equally bright regions above the other sunspots. No connection between line-of-sight velocity and heliocentric angle, θ, is apparent. For the coronal lines with log T $\approx$ 6.0 (6.4) the velocity is below 10 km s^{-1} in eleven out of twelve sunspots. This implies a marked change from low velocities in the corona to strong downflows in the sunspot transition region. To clarify the problem let us study the spatial distribution of the relative line-of-sight velocity in O V λ629, formed in the transition region and compare the results with those obtained for the low corona line Mg IX λ368, see Figures 3 and 4 (Plates L00 and L00), respectively. Figures 3 and 4 (Plates L00 and L00) confirm the results presented in Figure 2. Almost the entire area encircled with a yellow contour in the sunspot transition region is strongly redshifted, see Figure 3 (Plate L00), whereas the corresponding areas in Figure 4 (Plate L00) show little or no wavelength shift. This fascinating result deserves a few comments.

The observations are obtained with small to mod-

erate heliocentric angles and show that the vertical flow in the corona is too small to maintain a strong flow in the sunspot transition region. This suggests that the gas has to be supplied from regions surrounding the sunspot. Let us examine Figures 3 and 4 (Plates L00 and L00). Almost all sunspot regions in Figure 3 (Plate L00) contain one or a few prominent, strongly redshifted velocity channels, several of which extend from inside the sunspot to considerable distances from the sunspot. We note that plasmas at transition region temperatures may occur at considerable heights within the active region (e.g. Brekke, Kjeldseth-Moe, & Harrison 1997). Since the gas is moving away from the observer in the velocity channels that end in the sunspot, it seems likely that the gas is moving from regions located at a greater height outside the sunspots and towards the sunspot plume region. This interpretation is compatible with the results presented in Figure 3 (Plate L00) and with the low velocities observed in Figure 4 (Plate L00), where only NOAA 8076 shows a prominent, redshifted velocity channel. The present observations, interpreted in terms of gas at transition region temperature moving from greater height towards the sunspot plume, may be of interest in future studies of the suggestion that transition region structures are not physically connected to the coronal structures (Feldman 1983).

It is interesting to compare corresponding images in Figures 1 and 3 (Plates L00 and L00). We find that the enhanced line emission regions tend to be redshifted. For a few sunspots, such as NOAA 8076, there is good correspondence between redshift and peak line intensity, whereas in others, such as NOAA 8113, there is a marked difference between the location of the enhanced line emission and the most prominent, redshifted channels.

Above we have tacitly assumed that the wavelength shift is caused by material flow. We note that the observations may be compatible with an alternative interpretation of redshifts in the transition region lines, proposed by Hansteen, Maltby, and Malagoli (1996). Based on numerical simulations they find that episodic, magneto-hydrodynamic disturbances that originate in the corona and become nonlinear as they propagate towards the transition region may produce an overabundance of redshifts in the transition region lines, combined with small to moderate wavelength shifts in the coronal lines.

We would like to thank all the members of the large international CDS team for their extreme dedication in developing and operating this excellent instrument, the Michelson Doppler Imager team and T. Rimmele at the National Solar Observatory for permission to use their data and the Research Council of Norway for financial support. SOHO is a mission of international cooperation between ESA and NASA.

REFERENCES

Brekke, P., Kjeldseth–Moe, O., & Harrison, R. A. 1997, Sol. Phys., 175, 511

Brynildsen, N., Brekke, P., Fredvik, T., Haugan, S. V. H., Kjeldseth–Moe, O., Maltby, P., Harrison, R. A., & Wilhelm, K. 1998, Sol. Phys., in press

Brueckner, G. E., Bartoe, J.-D. F., & Van Hoosier, M. E.: 1977, in Proc. OSO–8 Workshop (Boulder: Lab. Atmospheric and Space Physics), 380

Feldman, U. 1983, ApJ, 275, 367

Foukal, P. V. 1976, ApJ, 210, 575

Foukal, P. V., Huber, M. C. E., Noyes, R. W., Reeves, E. M., Schmahl, E. J., Timothy, J. G., Vernazza, J. E., & Withbroe, G. L. 1974, ApJ, 193, L143

Gurman, J. B. 1993, ApJ, 412, 865

Hansteen, V., Maltby, P. & Malagoli, A. 1996 in R. D. Bentley & J. T. Mariska (eds.), Magnetic Reconnection in the Solar Atmosphere, ASP Conf. Ser. 111, 116

Harrison, R. A. et al. 1995, Sol. Phys., 162, 233

Kjeldseth-Moe, O. et al. 1988, ApJ, 334, 1066

Maltby, P. 1997, in B. Schmieder, J. C. del Toro Iniesta, & M. Vázques (eds.) Advances in the Physics of Sunspots, ASP Conf. Ser. 118, 91

Maltby, P., Brynildsen, N. , Brekke, P., Haugan, S. V. H., Kjeldseth–Moe, O., Wikstøl, Ø., & Rimmele, T. 1998, ApJ, 496, L117

Nicolas, K. R., Kjeldseth–Moe, O., Bartoe, J.-D. F., & Brueckner, G. E. 1982, Solar Phys., 81, 253

Noyes, R. W., Raymond, J. C., Doyle, J. G., & Kingston, A. E. 1985, ApJ, 297, 805

Scherrer, P. H. et al. 1995, Sol. Phys., 162, 129

This 2-column preprint was prepared with the AAS LaTeX macros v4.0.

Fig. 1.— Observed spatial distribution of Ne VI λ562 peak line intensity in twelve sunspot regions. Enhanced intensities are shown as dark regions. Areas with peak line intensity, I, larger than 2.5 and 5 times the average intensity, $\overline{I}$, are encircled by green and yellow contours, respectively. The images are oriented with north up, west to the right, and positions are given relative to the disk centre. The umbral and penumbral contours are shown.

Fig. 2.— Relative line-of-sight velocity, v, versus line formation temperature, T, in the area above the sunspot where the Ne VI λ562 peak line intensity $I > 5 \times \overline{I}$. The sunspots are ordered after increasing heliocentric angle, θ, see upper right hand corner for each sunspot.

Fig. 3.— Spatial distribution of the relative line-of-sight velocity in O V λ629. The velocities are measured relative to the average velocity in each image. Motion towards (away from) the observer is shown with blue (red) color. Green and yellow contours correspond to Ne VI λ562 peak line intensity, I (Ne VI), equal to 2.5 and 5 times the average intensity, $\overline{I}$ (Ne VI). For descriptions of positions, image orientation, and sunspot contours, see Figure 1.

Fig. 4.— Spatial distribution of the relative line-of-sight velocity in Mg IX λ368. The velocities are measured relative to the average velocity in each image. Motion towards (away from) the observer is shown with blue (red) color. Green and yellow contours correspond to Ne VI λ562 Å peak line intensity, I (Ne VI), equal to 2.5 and 5 times the average intensity, $\overline{I}$ (Ne VI). White pixels mark regions without data or regions where the uncertainty exceeds 10 km s^{-1}. For descriptions of positions, image orientation, and sunspot contours, see Figure 1.

Table 1: OBSERVED ACTIVE REGIONS

NOAA	Date	Days	No.[a]	θ^b (deg)
7973	1996 Jun 26	1	3	16
7981	1996 Aug 2	1	5	16
7986	1996 Aug 29	1	3	17
7999	1996 Nov 27 - 29	3	9	19 - 46
8011	1997 Jan 16 - 17	2	14	0 - 13
8073	1997 Aug 15-21	6	33	10 - 41
8076	1997 Aug 29-31	3	26	20 - 27
8083	1997 Sep 6 - 13	4	31	35 - 64
8085	1997 Sep 15	1	4	44
8108	1997 Nov 18 - 21	2	20	22 - 24
8113	1997 Nov 29 - Dec 5	4	45	19 - 43
8123	1997 Dec 17 - 18	2	16	20 - 32

[a] No. = Number of rasters

[b] The angle θ = heliocentric angle.

Table 2: OBSERVED EMISSION LINES

Selected Line	λ (Å)	log T (K)	Second line[a]	λ (Å)
He I	522.20	4.3	Ne IV	521.8
He I	584.33	4.3		
O III	599.60	5.0		
O IV	554.51	5.2	O IV	554.08
O V	629.73	5.4	Ar VII	630.30
Ne VI	562.80	5.6	Ne VI	562.71
Mg VIII	315.04	5.9	Mg VI	314.6
Mg IX	368.07	6.0	Mg VII	367.7
Fe XIV	334.17	6.2	N IV	335.05
Fe XVI	360.76	6.4		361.25

[a] Second most intense line(s) within the spectral window

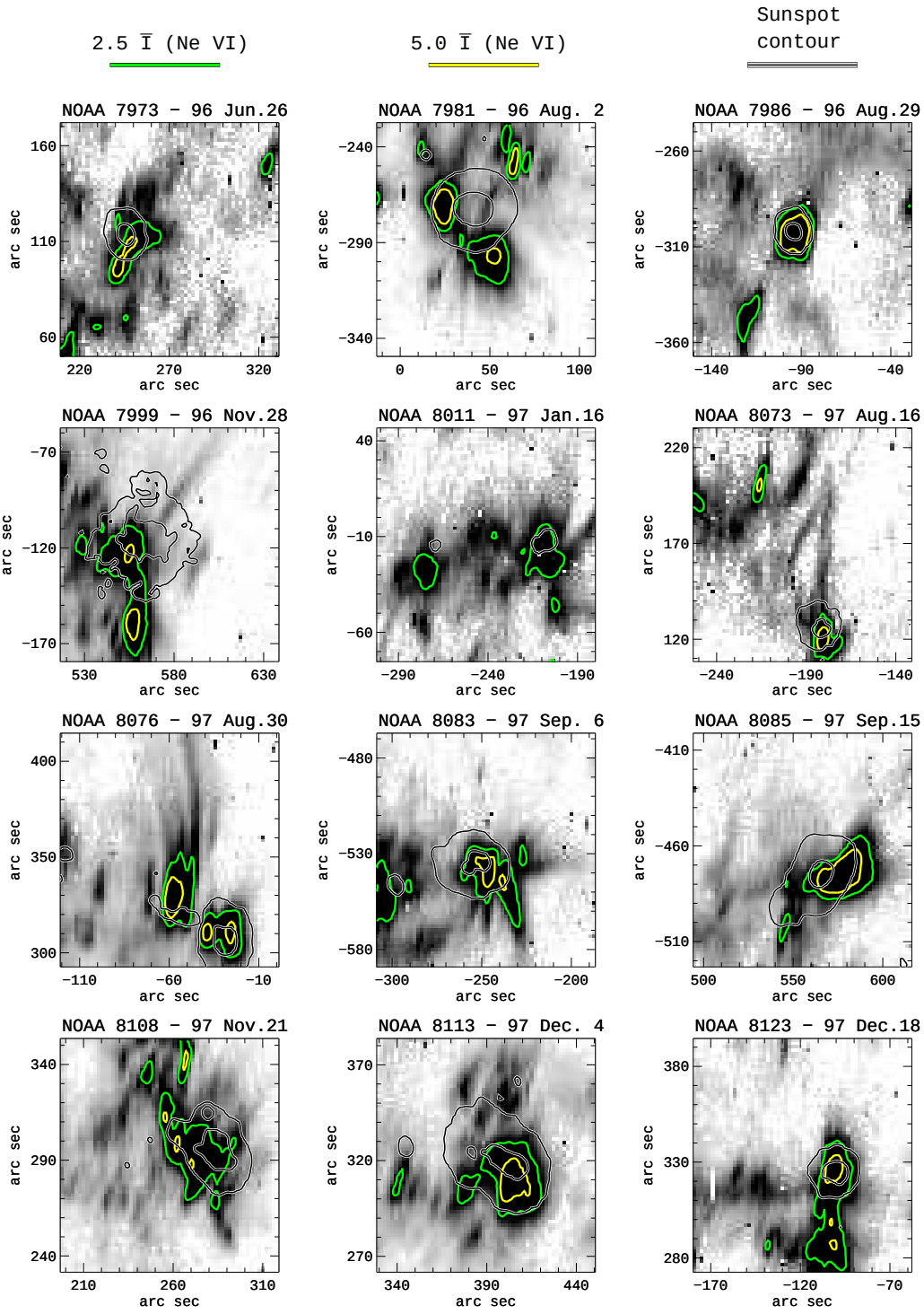
2.5 Ī (Ne VI)
5.0 Ī (Ne VI)
Sunspot contour
NOAA 7973 – 96 Jun.26
NOAA 7981 – 96 Aug. 2
NOAA 7986 – 96 Aug.29
NOAA 7999 – 96 Nov.28
NOAA 8011 – 97 Jan.16
NOAA 8073 – 97 Aug.16
NOAA 8076 – 97 Aug.30
NOAA 8083 – 97 Sep. 6
NOAA 8085 – 97 Sep.15
NOAA 8108 – 97 Nov.21
NOAA 8113 – 97 Dec. 4
NOAA 8123 – 97 Dec.18
arc sec

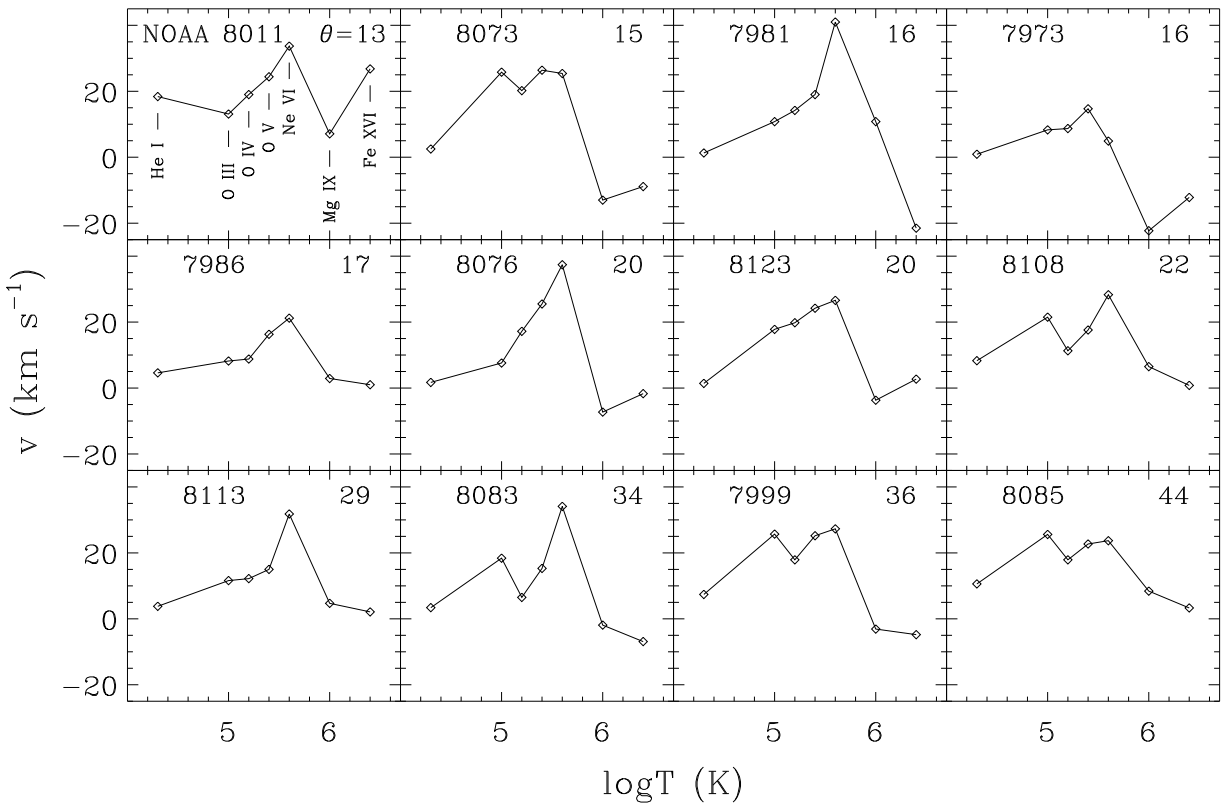
NOAA 8011 θ=13
8073 15
7981 16
7973 16
7986 17
8076 20
8123 20
8108 22
8113 29
8083 34
7999 36
8085 44
He I —
O III —
O IV —
O V —
Ne VI —
Mg IX —
Fe XVI —
v (km s−1)
logT (K)

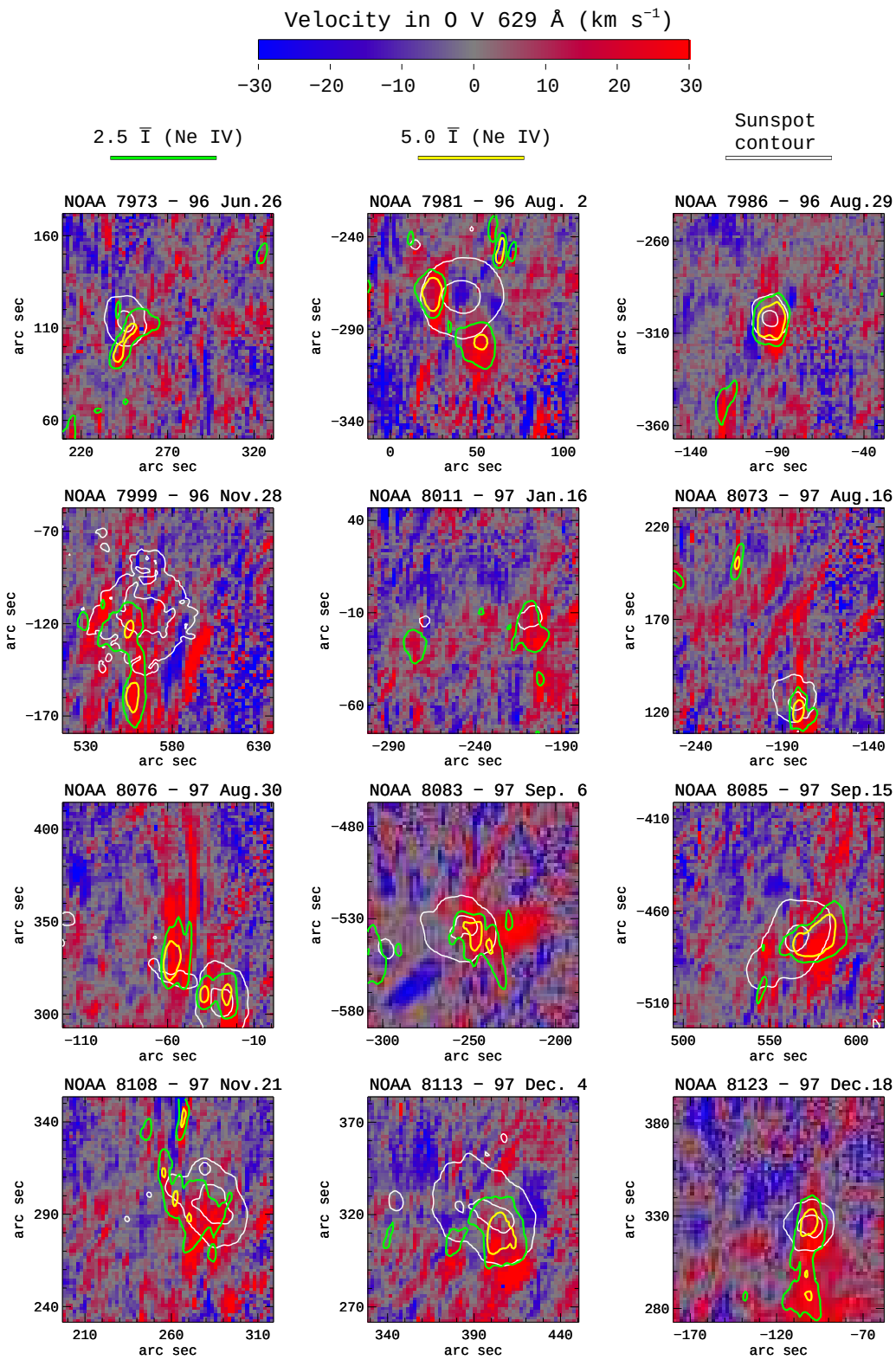
Velocity in O V 629 Å (km s^{-1})
−30 −20 −10 0 10 20 30
2.5 $\bar{I}$ (Ne IV)
5.0 $\bar{I}$ (Ne IV)
Sunspot contour
NOAA 7973 – 96 Jun.26
NOAA 7981 – 96 Aug. 2
NOAA 7986 – 96 Aug.29
NOAA 7999 – 96 Nov.28
NOAA 8011 – 97 Jan.16
NOAA 8073 – 97 Aug.16
NOAA 8076 – 97 Aug.30
NOAA 8083 – 97 Sep. 6
NOAA 8085 – 97 Sep.15
NOAA 8108 – 97 Nov.21
NOAA 8113 – 97 Dec. 4
NOAA 8123 – 97 Dec.18
arc sec

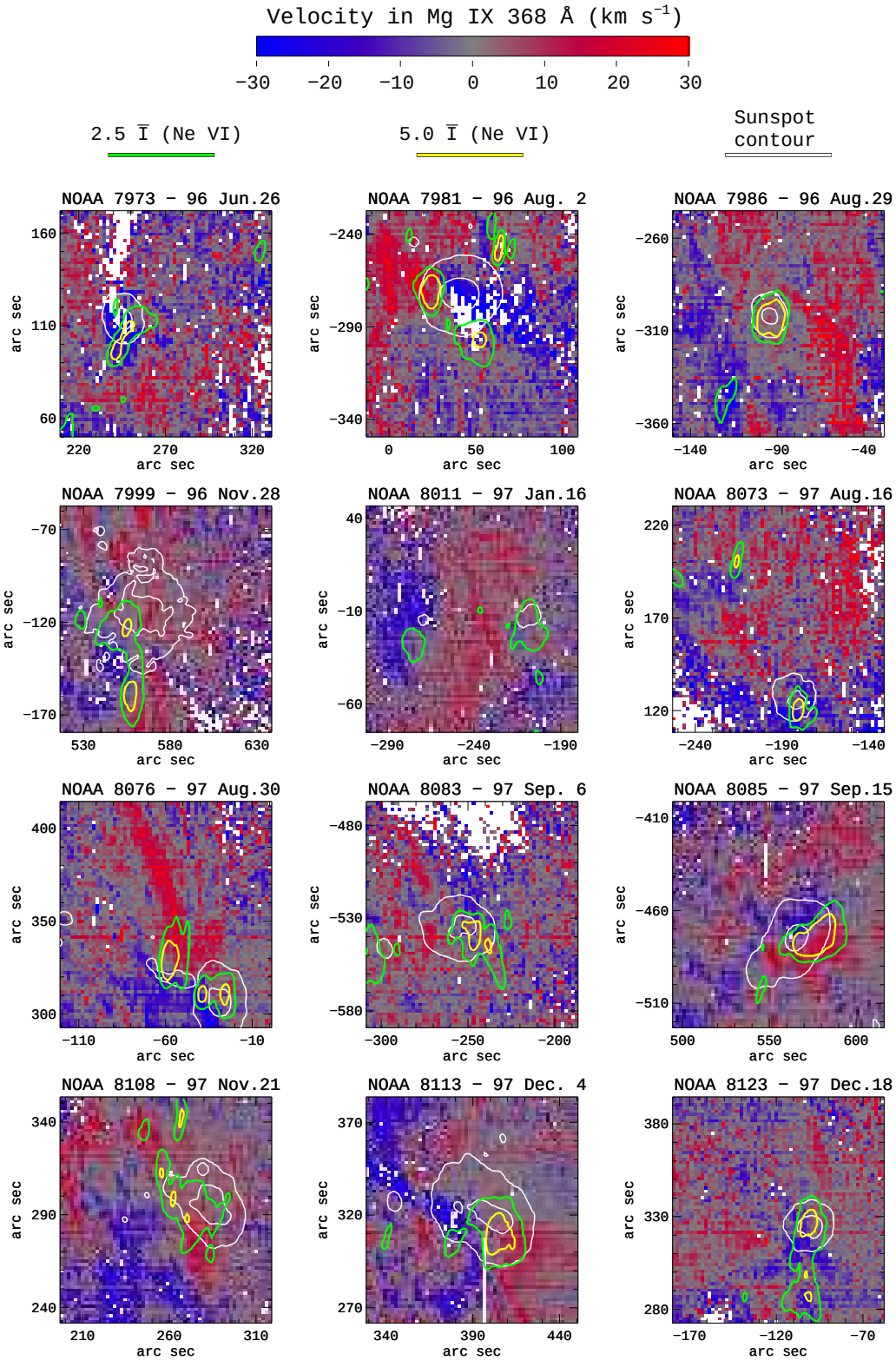
Velocity in Mg IX 368 Å (km s^{-1})
−30 −20 −10 0 10 20 30
2.5 Ī (Ne VI)
5.0 Ī (Ne VI)
Sunspot contour
NOAA 7973 – 96 Jun.26
NOAA 7981 – 96 Aug. 2
NOAA 7986 – 96 Aug.29
NOAA 7999 – 96 Nov.28
NOAA 8011 – 97 Jan.16
NOAA 8073 – 97 Aug.16
NOAA 8076 – 97 Aug.30
NOAA 8083 – 97 Sep. 6
NOAA 8085 – 97 Sep.15
NOAA 8108 – 97 Nov.21
NOAA 8113 – 97 Dec. 4
NOAA 8123 – 97 Dec.18
arc sec